

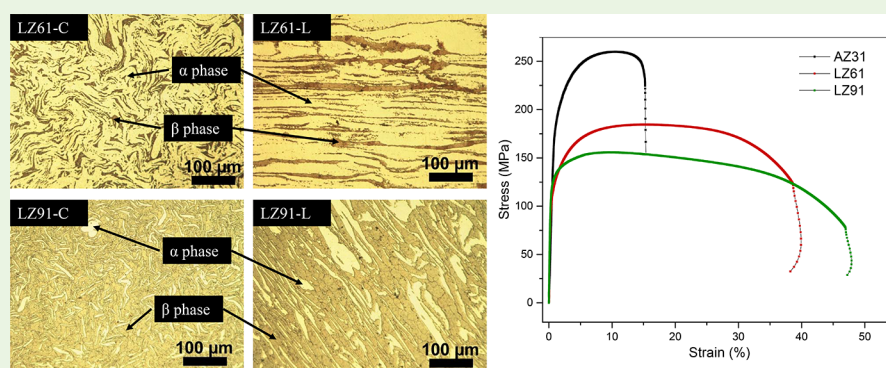
# In Vitro and in Vivo Evaluation of Multiphase Ultrahigh Ductility Mg–Li–Zn Alloys for Cardiovascular Stent Application

Jingyao Wu,<sup>†,‡</sup> Daoli Zhao,<sup>§</sup> John M. Ohodnicki,<sup>†,‡</sup> Boeun Lee,<sup>†</sup> Abhijit Roy,<sup>†,‡</sup> Raymon Yao,<sup>†</sup> Shauna Chen,<sup>||</sup> Zhongyun Dong,<sup>||</sup> William R. Heineman,<sup>§</sup> and Prashant N. Kumta<sup>\*,†,‡,||,§,||</sup>

<sup>†</sup>Department of Bioengineering, <sup>‡</sup>McGowan Institute of Regenerative Medicine, <sup>||</sup>Department of Mechanical Engineering and Materials Science, and <sup>§</sup>Department of Chemical and Petroleum Engineering, University of Pittsburgh, Pittsburgh, Pennsylvania 15261, United States

<sup>§</sup>Department of Chemistry, University of Cincinnati, Cincinnati, Ohio 45221, United States

<sup>||</sup>Department of Internal Medicine, University of Cincinnati, Cincinnati, Ohio 45267, United States



**ABSTRACT:** Magnesium alloys have been extensively studied as a novel biodegradable metallic material for cardiovascular stent application. However, the ductility limitation of magnesium alloy has been a key issue for biodegradable stents applications. In this study, two different multiphase ultrahigh ductility Mg–Li–Zn alloys, LZ61 and LZ91, are fabricated in the form of extruded rods and evaluated both in vitro and in vivo. The microstructure, mechanical properties and in vitro degradation are evaluated as well as in vitro cytotoxicity. The in vivo degradation, tissue response, and systematic toxicity are evaluated in a mouse subcutaneous model. Measurements show that LZ61 and LZ91 exhibit more than 40% elongation at fracture without significantly compromising the strength. Both in vitro and in vivo degradation showed low degradation rates for LZ61 but high degradation rate for the LZ91 alloy. Excellent biocompatibility is observed both in vivo and in vitro for LZ61 and LZ91. In summary, this study successfully demonstrates that the ultraductility multiphase Mg–Li–Zn alloy has the potential to be used for stent applications. Compared to LZ91, the LZ61 alloy shows better balance of mechanical properties, corrosion resistance, and biocompatibility, indicating its promise for cardiovascular stent applications.

**KEYWORDS:** magnesium alloy, biodegradable, Mg–Li, high-ductility, hydrogen sensor

## 1. INTRODUCTION

As a novel biodegradable metallic material, magnesium-based alloys have been extensively studied for a variety of stent applications over the past 10 years. Magmaris bioresorbable scaffold, which is the first magnesium vascular stent that received a CE mark in 2016, has shown promising clinical outcomes in a series of clinical trials. A variety of magnesium-based alloy systems have been developed to meet the design requirements of stent applications. The main principles in the core design of biodegradable magnesium based alloys are: (1) achieve appropriate biodegradation rate in an aqueous environment; (2) show good ductility to achieve high plastic deformation to endure the stent crimping and expansion processes occurring during stent deployment; (3) display adequate strength to maintain the mechanical support against the vascular wall during degradation of the device; and (4)

exhibit no significant short-term and long-term toxicity of the alloying elements as well as the related degradation products. Mg–Al<sup>1–3</sup> and Mg–Re<sup>4–7</sup> are the major magnesium alloy systems that have been studied for stent applications to date, and both alloy systems have showed good corrosion resistance and biocompatibility. However, because of the hexagonal close packed (HCP) crystal structure of magnesium, the ductility of these magnesium-based alloys is severely limited. Most of the alloys reported to date in the literature, exhibit an elongation around 10–30% at fracture posing difficulties in the stent design and manufacture of magnesium stents.<sup>8,9</sup> For currently used nondegradable stents, the materials usually possess an

Received: November 6, 2017

Accepted: December 22, 2017

Published: December 22, 2017

excellent balance of strength and ductility. 316L stainless steel, for example, exhibits an elongation of 55% at fracture.<sup>10</sup> Difficulties of fine magnesium tube drawing and the fracture of magnesium stents after balloon expansion has been reported in previous studies.<sup>11–13</sup> Therefore, the development of high ductility magnesium alloy would be considered a great benefit for the next generation magnesium stents.

Mg–Li alloys were first developed by NASA as an ultralight alloy for aerospace applications in 1960s.<sup>14</sup> The microstructure of the Mg–Li alloys depends on the Li content. With less than 5.7 wt % of Li, the binary alloy comprised single phase  $\alpha$ , exhibiting the HCP structure; with more than 10.3 wt % Li, however, the Mg–Li alloy exhibits single-phase  $\beta$  belonging to the BCC structure. Both the  $\alpha$  phase and  $\beta$  phases coexist when the Li content is between 5.7% and 10.3%. Several studies have been conducted on the single phase,  $\alpha$  Mg–Li alloys for biomedical application. For example, LAE442 alloy has been extensively studied as an orthopedic implant.<sup>15–17</sup> Mg–Li–Ca alloys were also investigated for biomedical applications.<sup>18,19</sup> Compared to the  $\alpha$  phase, Mg–Li alloy, the  $\beta$  phase of Mg–Li alloy is more attractive because of the unique BCC structure especially for biodegradable stents and other applications requiring high ductility material. However, due to the inferior mechanical properties of the single  $\beta$  phase Mg–Li alloy, no study has been reported related to the biomedical applications of single phase  $\beta$  Mg–Li alloy. With a mixture of  $\alpha$  and  $\beta$  phases, the multiphase Mg–Li alloys exhibit ultrahigh ductility while also maintaining relatively high strength, and therefore would be more amenable for load-bearing biomedical applications. Zhou et al. first reported the long-term in vitro hydrogen evolution of multiphase Mg–Li–Al–(Re) alloys, and demonstrated the stable degradation of the LA92 alloy as well as higher corrosion of Mg–Li–Al–Re alloys.<sup>20</sup> A more detailed study was later published demonstrating the superior mechanical property, stable degradation, and acceptable biocompatibility of Mg–Li–Al–(Re) alloys.<sup>21</sup> Zeng et al. also investigated the corrosion mechanism of multiphase Mg–Li–Ca alloy in Hank's solution.<sup>22</sup> To the best of our knowledge, however, there is no comprehensive in vitro and in vivo study reported to date investigating the mechanical properties, degradation and biocompatibility of multiphase Mg–Li alloys containing Zn. In this context, Mg–Li–Zn alloy has been proposed as an ultralight metal for industrial aerospace and automobile applications. The study has extensively focused on mechanical properties and plastic deformation of Mg–Li–Zn alloys.<sup>23–26</sup> A recent publication has studied the three single  $\alpha$  phase Mg–Li–Zn alloy and three multiphase Mg–Li–Zn alloys for stent application, mechanical properties and in vitro degradation were discussed demonstrating the potential of Mg–Li–Zn alloy for stent application.<sup>27</sup>

In the present study herein, two multiphase Mg–Li–Zn ternary alloys, Mg-6Li-1Zn (LZ61) with a higher percentage of the specific single phase of the  $\alpha$  phase and Mg-9Li-1Zn (LZ91) with a higher percentage of the cubic  $\beta$  phase, were accordingly designed and evaluated for cardiovascular stent applications. The alloying elements were selected based on the design principle mentioned above. Besides alloying with Li, as one of the human essential elements, Zn is also chosen to further improve the strength of the Mg–Li system via solid solution strengthening mechanism. Furthermore, our previous first-principles study executed also demonstrated that the addition of Zn into the magnesium alloy will lead to enhancement of the ductility of these alloys.<sup>28</sup> The goal of

this study is thus, to demonstrate the following: (1) the multiphase Mg–Li alloy will likely exhibit superior mechanical properties suitable for stent application when compared to the currently used common Mg alloy systems; (2) the coexistence of the  $\alpha$  and  $\beta$  dual phases will not alter the in vitro and in vivo degradation rates significantly; (3) with a simple chemical metallic composition, the Mg–Li–Zn alloys will display not only excellent cytocompatibility but also elicit no noticeable trace of local and systemic toxicity. In the present study, the microstructure, tensile strength, in vitro degradation were also accordingly investigated. Consequently, human umbilical vein endothelial cells (HUVEC) and human aorta smooth muscle cells (HASMC) were selected to evaluate the cytotoxicity of the selected Mg–Li–Zn alloys in vascular cells. Furthermore, we report herein for the first time to the best of our knowledge, the in vivo degradation, hydrogen evolution, and systemic toxicity of these multiphase Mg–Li alloys in a mouse subcutaneous model.

## 2. MATERIALS AND METHODS

**2.1. Materials Fabrication and Characterization.** Mg-6Li-1Zn (LZ61) and Mg-9Li-1Zn (LZ91) in the form of extruded rods (20 mm in diameter) were fabricated with the assistance from Xi'an SiFang EM CO., LTD (Xi'an, China). 99.9% pure Mg as drawn rods, and AZ31 extruded rods were purchased from Goodfellow (Coraopolis, PA) and used as controls. The actual chemical composition of the fabricated Mg–Li–Zn alloys was then verified by inductively coupled plasma optical emission spectroscopy (ICP-OES, iCAP duo 6500 Thermo Fisher, Waltham, MA). The formation and presence of the individual phases was identified by X-ray diffraction using the X-ray diffractometer (Philips X'Pert PRO diffractometer), employing Cu  $K\alpha$  ( $\lambda = 1.54056 \text{ \AA}$ ) radiation with a Si detector (X'celerator). The X-ray generator was operated at 45 kV employing 40 mA current in the  $2\theta$  range from 10 to 90°.

**2.2. Microstructure Characterization.** To observe the microstructure of the fabricated Mg–Li–Zn alloys, we sliced round plate samples ( $\phi = 10 \text{ mm} \times 2 \text{ mm}$ ) by lathe from the center of the extruded rods. All the samples were ground with SiC abrasive sandpapers up to 1200 grit and polished initially with monocrystalline diamond suspension spray (1  $\mu\text{m}$ , Buehler) and finally with Masterprep Alumina Suspension (0.05  $\mu\text{m}$ , Buehler). The samples were etched using a solution of 5 mL of acetic acid, 6 g of picric acid, 10 mL of water, and 100 mL of ethanol (picral). Microstructures of the polished and etched samples were then observed under a Nikon Optiphot microscope (Nikon, Tokyo, Japan).

**2.3. Mechanical Characterization.** Tensile testing was performed using the extruded Mg–Li–Zn alloys employing commercially obtained AZ31 plate (Alfa Aesar, Tewksbury, MA) as the control. Tensile bars were machined along the axis direction of the extruded rods by CNS machine. The size of the tensile bars was determined as per ASTM E8/E8M-11 standard with 12.7 mm gauge length and 3 mm  $\times$  3 mm gauge area. For each sample, the stress–strain curve was generated by Instron 5969 testing system (Instron, Norwood, MA) equipped with an extensometer (Instron 2630 series, Norwood, MA) measuring the elongation. Three typical stress–strain curves obtained from each group were used to calculate the yield strength (YS), ultimate strength (UTS) and elongation at fracture (EL) using the Bluehill 3 Testing Software for Mechanical Testing Systems (Instron, Norwood, MA). Average and standard deviations of the three samples were calculated for each group.

**2.4. Electrochemical Analysis.** All the alloy samples in the shape of disks (10 mm in diameter and 2 mm in thickness) were mounted in epoxy with only one side of the flat surface exposed. The edge of the sample was then sealed using nail polish. The alloy surface was ground using SiC abrasive sand papers up to 1200 grit. A three-electrode cell setup was employed for electrochemical corrosion testing utilizing platinum wire as the auxiliary electrode, Ag/AgCl as the reference

electrode and the epoxy-mounted sample serving as the working electrode. Each sample was subsequently immersed in Hank's balanced salt solution (HBSS) for at least 10 min to reach a stable open circuit potential. Potentiodynamic polarization (PDP) plots were obtained in 37 °C HBSS with an electrochemical workstation (CHI 604A, CH Instruments, Inc., Austin, TX). All the samples were tested employing a scan rate of 1 mV/s within a potential window of ~500 mV above and below the open circuit potential. The corrosion potential,  $E_{\text{corr}}$ , the corrosion current density,  $i_{\text{corr}}$ , and corrosion rate,  $CR_{\text{corr}}$ , were then calculated following the method described in ASTM-G102-89.

**2.5. Immersion Test.** Immersion test was conducted to evaluate the in vitro degradation of Mg–Li–Zn alloys based on ASTM standard G31–12a. Round plate samples ( $\phi = 10 \text{ mm} \times 2 \text{ mm}$ ) were ground with SiC abrasive sand papers up to 1200 grit. All the samples were then sonicated in ethanol, weighed and sterilized under UV. Each sample was immersed in HBSS in a 50 mL conical centrifuge tubes. The ratio of HBSS volume to sample surface area is 0.20 mL/mm<sup>2</sup>. All the samples were kept in 37 °C. After immersion for 1, 3, and 5 weeks, the samples were retrieved from the buffer media, washed in DI water, ethanol and dried in air. The corrosion products were removed by immersion in solution of 200 g of chromium trioxide, 10 g of silver nitrate, and 1000 mL of water for 10 min. The samples were then washed in DI water and ethanol, dried in air, and weighed. The corrosion rate was calculated based on the mass loss utilizing the equation given below<sup>7</sup>

$$\text{corrosion rate (mm/year)} = K \frac{W}{ATD} \quad (1)$$

Where, the constant  $K$  is  $3.65 \times 10^3$ ,  $W$  is mass loss (g),  $A$  is the surface area of each sample (cm<sup>2</sup>),  $T$  is the immersion time (day), and  $D$  is the density of each alloy (g/cm<sup>3</sup>). The sample surface after removing the corrosion product was observed by scanning electron microscopy (SEM; JSM6610LV, JEOL).

**2.6. In Vitro Cytotoxicity Evaluation.** **2.6.1. Cell Culture and Extract Preparation.** Human aorta smooth muscle cells (HASMC) (ScienCell Research Laboratories #6110) and human vascular endothelial cells (HUVEC) (ATCC #PCS-100-010) were cultured in smooth muscle cell medium (SMCM) (ScienCell Research Laboratories) and endothelial cell growth medium (EGM-2) (EGM-2 BulletKit, Lonza Biosciences), respectively. The samples were ground utilizing SiC abrasive sand papers up to 1200 grit, sterilized for 30 min by exposure to UV radiation for each side and then immersed in cell culture medium for 72 h in a standard cell culture incubator. The specimen surface area to extraction medium ratio was maintained at 1.25 cm<sup>2</sup>/mL in accordance with EN ISO standard 10993–12:2004. This extraction ratio was designated as 100% extract. Extracts were sterile filtered using a 0.2  $\mu\text{m}$  syringe filter before being added to the cells. Low concentration extracts were prepared by diluting the 100% extract into 75, 50, 25, and 10% with cell culture medium.

**2.6.2. Indirect MTT Assay.** Indirect MTT assay were conducted following the same procedure described in previous publications from our group.<sup>7,29</sup> Briefly, the cells were seeded in 96-well plate at a cell density of 2000/well for HASMC and 4000/well for HUVEC and incubated for 12 h. Following this, 75, 50, 25, and 10% extracts were added with normal cell culture medium serving as the negative control, whereas 10% DMSO cell culture medium served as the positive control. The well plates were incubated for 1 day and 3 days respectively, and analyzed by Synergy 2 Multi-Mode Microplate Reader (Bio-Tek Instruments, Winooski, VT).

**2.6.3. Live/Dead Staining and DAPI&F-Actin Staining.** In addition to the tests above, live/dead staining was performed to investigate the cell viability while DAPI&F-actin staining was performed to image the cell morphology. Cells with a cell density of 2000/well for HASMC and 4,000/well for HUVEC were seeded in 48-well plates and accordingly incubated in 25% extract for 3 days. LIVE/DEAD viability/cytotoxicity kit (Invitrogen Inc., Karlsruhe, Germany) was used to stain the live and dead cells to glow green (ethidium homodimer-1) and red (calcein-AM), respectively. For DAPI&F-actin staining, DAPI (AppliChem, Darmstadt, Germany) served as the

fluorescent probe for observing DNA (blue), and rhodamine phalloidin served as the fluorescent probe to label the F-actin (red).

**2.6.4. Cell Apoptosis and Cell Cycle Assay.** The effect of the degradation products on cell apoptosis and cell cycle was evaluated by culturing 50 000 HASMC/well or 100 000 HUVEC/well in 6-well plates in 25% extract for 24 h. For the cell cycle study, the cells were cultured in serum-free medium for 24 h for synchronization. FITC Annexin V Apoptosis Detection Kit I (BD Biosciences, USA) was used to detect the early apoptosis and late apoptosis. Propidium Iodide (PI) (PI/RNase Staining Buffer, BD Biosciences, USA) was used to measure the DNA content and evaluate the percentage of cells in each cell cycle phase.

**2.7. Procedures for Laboratory Mice Implantation.** Specific pathogen-free female athymic nude mice were purchased from Harlan Laboratory (Indianapolis, IN) and used in this study when they were 8–10 weeks of age. The mice were maintained in a facility approved by the American Association for Accreditation of Laboratory Animal Care and in accordance with current regulations and standards of the U.S. Department of Agriculture, U.S. Department of Health and Human Services, and NIH. The animal studies were approved by the Institutional Animal Care and Use Committee (IACUC) and executed according to the specific IACUC guidelines.

The in vivo corrosion of LZ61, LZ91, pure Mg and AZ31 was evaluated in a subcutaneous model in mice as detailed in our previous studies.<sup>7,29,30</sup> Discs (5 mm diameter and 1 mm thickness) were sectioned from the extruded rods of LZ61, LZ91, pure Mg and AZ31 alloys and were then sonicated in acetone, distilled water and finally, air-dried. The pellets were placed in 70% ethanol for 5 min, rinsed with Dulbecco's phosphate buffer saline (DPBS, KCl 2.7 mM, KH<sub>2</sub>PO<sub>4</sub> 1.5 mM, NaCl 138 mM, Na<sub>2</sub>HPO<sub>4</sub> anhydrous 8.1 mM, pH 7.0), and then irradiated under UV light allowing for 20 min exposure on each side of the discs. The samples (6 mice/sample type) were placed subcutaneously into the mice. For the surgery procedure, all the mice were anesthetized with isoflurane and sterilized, and a small skin incision was made to create a subcutaneous pocket on the back of the mouse. The Mg alloy disc was then inserted into the pocket, and the incision was closed with surgical staples (Autoclip, Clay Adama) which was then subsequently removed following 2 weeks after the surgery. The mice were housed under controlled conditions and maintained with a standard diet and water. Gas bubble was measured twice a week using calipers and the specific bubble volume (mm<sup>3</sup>) was calculated according to the formula: (width<sup>2</sup> × length)/2, a formula that was routinely used in measurement of subcutaneous tumor volumes in mice.<sup>31</sup> The mice were accordingly weighed twice a week and sacrificed approximately at 4 and 12 weeks, respectively. The implants were weighed before and after implantation following which, the weight loss was calculated and converted to corrosion rate employing the same equation used to determine corrosion in the immersion test. The in vivo corrosion rates were then further compared with the in vitro corrosion rates.

**2.8. Histology Analysis.** For histological evaluations, the skin tissue adjacent to the implants and major organs were sampled, fixed in neutral buffered 4% formalin solution, embedded in paraffin, sectioned (4  $\mu\text{m}$ ), and stained accordingly with hematoxylin and eosin (H&E).

**2.9. H<sub>2</sub> Measurement by Amperometric H<sub>2</sub> Sensor.** Amperometric H<sub>2</sub> measurements were performed using a H<sub>2</sub> microsensor (H<sub>2</sub> 50, 50  $\mu\text{m}$  tip diameter from Unisense, Aarhus, Denmark). The calibration and the appropriate conversion from the H<sub>2</sub> microsensor current to the specific concentration used was similar to our earlier published works.<sup>32–34</sup> For in vivo measurements, the anesthetized mice were immobilized on a heated swiveling table. The microsensor was then appropriately positioned with a micro-manipulator.<sup>33,34</sup> Measurements were then taken by touching the sensor tip on the skin above the gas cavity near the implant area. The current obtained from the H<sub>2</sub> sensor was then converted to a regional H<sub>2</sub> concentration using a calibration curve generated from known levels of H<sub>2</sub> in water prepared by diluting the H<sub>2</sub> saturated water.

**2.10. Statistical Analysis.** The obtained results were expressed as the mean  $\pm$  standard deviation. One-way ANOVA was conducted to

determine the differences between the different groups of samples with Bonferroni Procedure as the post hoc test. Two-way ANOVA was performed for MTT test with Bonferroni procedure as post hoc test. Statistical significance was defined as  $p < 0.05$ . Statistical analysis was performed utilizing the IBM SPSS Statistics 23 package for Windows.

### 3. RESULTS

**3.1. Microstructure of Mg–Li–Zn Alloy.** Mg–Li–Zn alloys were first verified by measuring the chemical composition and observing the microstructure. Table 1 shows the ICP

**Table 1. Chemical Composition of Mg–Li Zn Alloys**

nominal composition (wt %)	chemical composition (wt %)		
	Li	Zn	Mg
Mg-6Li-1Zn	6.11 ± 0.13	0.92 ± 0.08	Bal.
Mg-9Li-1Zn	9.00 ± 0.14	0.96 ± 0.04	Bal.

results of the actual chemical composition of each Mg–Li–Zn alloy. The elemental compositions of most of the elements are close to the nominal composition, and the impurities level of each alloy was low, avoiding the potential rapid corrosion rate caused by microgalvanic corrosion. The optical images (Figure 1a–d) of the microstructure clearly show the presence of a mixture of  $\alpha$  ( $\text{Li}_{0.92}\text{Mg}_{4.08}$ ) and  $\beta$  ( $\text{Li}_3\text{Mg}_7$ ) phases with the lighter colored area representing the  $\alpha$  phase and the darker colored area representing the  $\beta$  phase, respectively. In Figure 1, both the cross-section and longitudinal sections of LZ61 images of the microstructure (Figure 1a, b) show a higher percentage of the lighter colored area ( $\alpha$  phase), whereas the LZ91 images of microstructure (Figure 1c, d) show a much higher percentage of the darker colored area ( $\beta$  phase). The cross-section of both alloys showed a typical fibrous extrusion texture and the grains were extremely elongated in the longitudinal direction. The optical images of the microstructure were also further analyzed by using the ImageJ software (v1.51h). For the LZ61 alloy, the area of the  $\beta$  phase in percentage of the whole image was determined to be 27.56% for the cross-sectional image and 29.63% for the image corresponding to the

longitudinal section. For the LZ91 alloy, the area of the  $\beta$  phase in percentage of the whole image was 70.72% for the cross-sectional image and 89.15% for the corresponding image of the longitudinal section. The X-ray diffraction analysis result (Figure 1e) further confirms the coexistence of both the phases. The peaks representing the  $\beta$  phase were significantly more intense in the LZ91 pattern than in the LZ61 diffraction pattern further confirming and indicating the presence of a higher percentage of the  $\beta$  phase. The X-ray diffraction trace also exhibited the diffraction peak of the MgZn intermetallic.

**3.2. Mechanical Properties of the Generated Mg–Li–Zn Alloy.** It is well-known that for balloon expandable stents, the routine stent delivery method requires the system to exhibit and demonstrate the capability to undergo plastic deformation. At the same time, higher strength is preferred for the system to maintain the mechanical support against the vessel wall after stent delivery. To screen the candidate material, researchers usually select a tensile test to evaluate both the strength and the ductility of the selected material.<sup>21,35,36</sup> Figure 2 shows the mechanical properties of the Mg–Li–Zn alloys compared with the commercial AZ31 alloy used as the control. Typical stress–strain curves obtained from the tensile test are plotted in Figure 2a. LZ61 and LZ91 alloys showed much higher strain before fracture when compared to the AZ31 control alloy which exhibited a steep increase in the strength. Our results clearly demonstrate that, with the addition of Li, the ductility of the Mg–Li multiphase alloys is significantly improved ( $p < 0.05$ ) as shown in Figure 2b. The LZ61 alloy containing 6 wt % Li exhibits 44 ± 2% elongation before fracture which is more than twice the elongation of AZ31 alloy (17 ± 2%). However, increasing the Li content to 9 wt % only marginally increased the ductility of the multiphase Mg–Li alloy with elongation before fracture reaching 47 ± 3%. Moreover, it can be seen that expectedly, the significant increase in ductility resulted in compromising the strength of the multiphase Mg–Li alloy likely due to Li being a softer metal. Accordingly, the yield strength (YS) of the LZ61 and LZ91 decreased to 119 ± 11 MPa and 115 ± 3 MPa, respectively, whereas the AZ31 alloy displays a YS of 158 ± 20 MPa. A similar trend is observed for

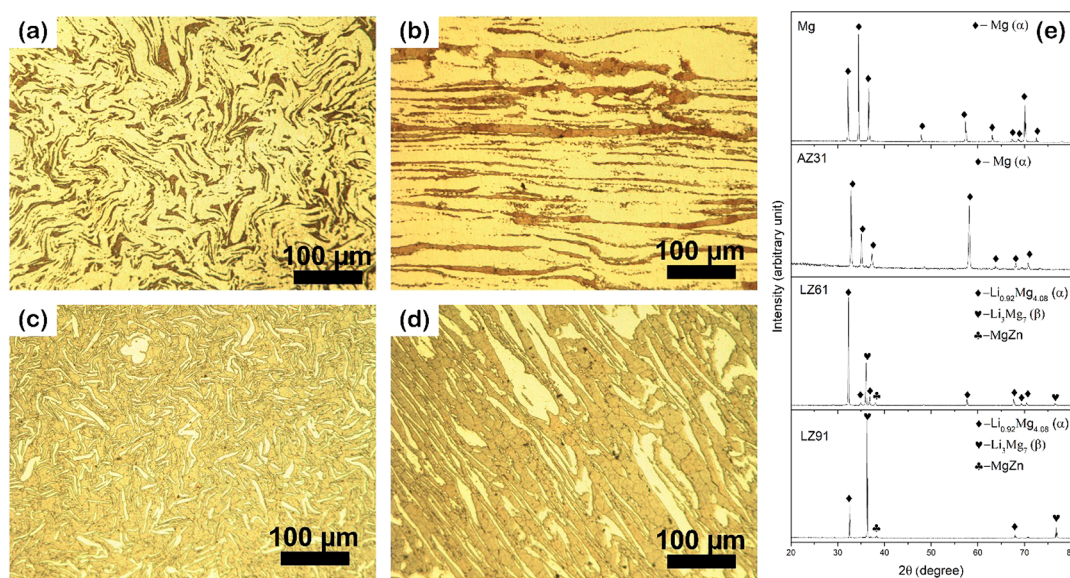


**Figure 1.** Microstructure of the Mg–Li–Zn alloys. LZ61 alloy (a) cross-section, (b) longitudinal section, LZ91 alloy (c) cross-section, (d) longitudinal section. (e) XRD pattern of Mg–Li–Zn alloys (please note the ordinate represents logarithm of intensity in arbitrary units).

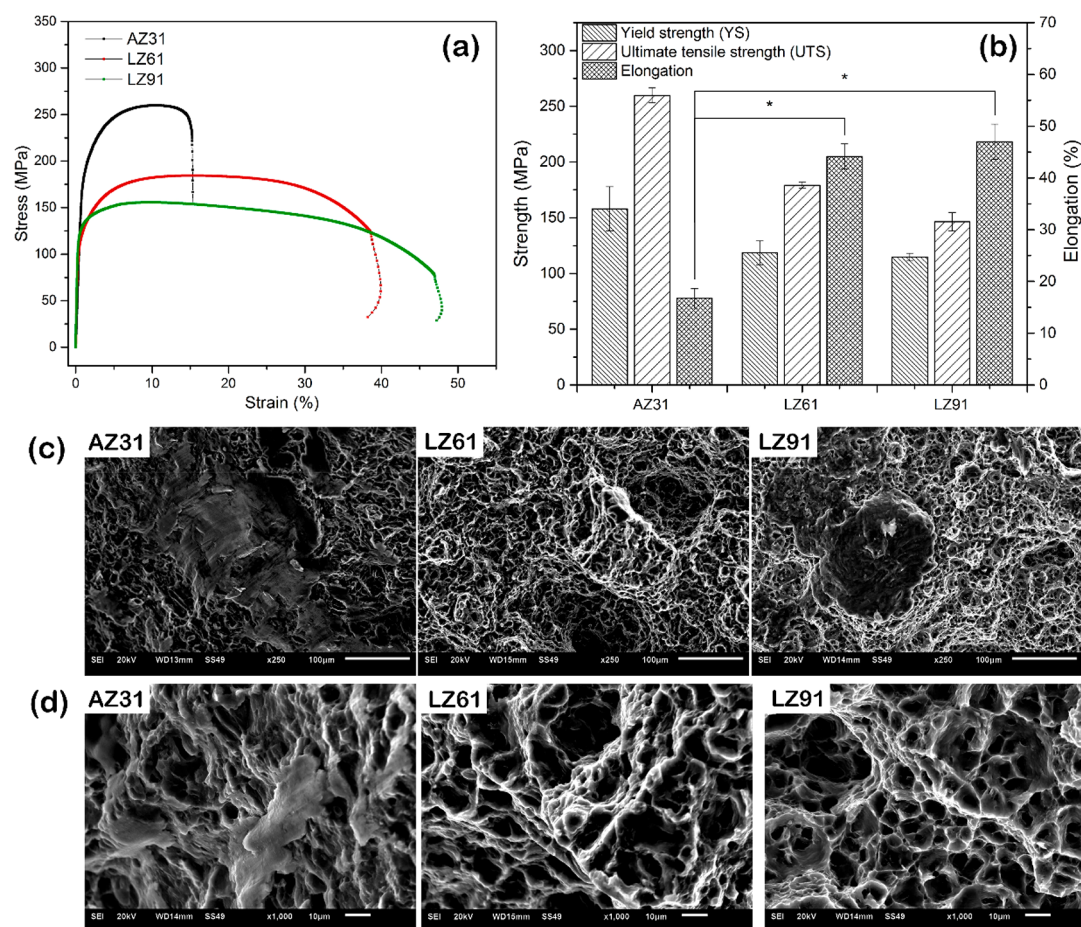


**Figure 2.** Mechanical properties of Mg–Li–Zn alloys. (a) Typical stress–strain curves. (b) Tensile strength of Mg–Li–Zn alloys. \*denotes a significant difference between LZ61 and AZ31, LZ91 and AZ31 in ductility ( $p < 0.05$ ,  $n = 3$ ). (c, d) Scanning electron fractography of the tensile bar fracture surface (c) 250 $\times$  (d) 1000 $\times$ .

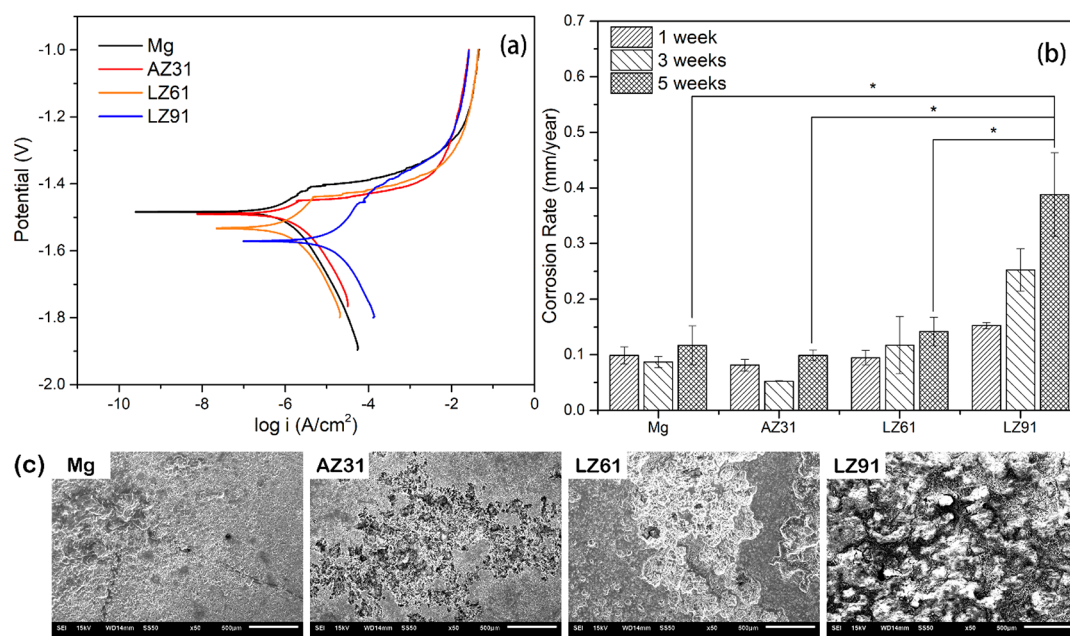


**Figure 3.** (a) Potentiodynamic polarization curves of LZ61, LZ91, pure Mg and AZ31 alloy in HBSS. (b) In vitro degradation rate of Mg–Li alloys in Hank's solution by immersion test. \*denotes a significant difference between LZ91 and other groups ( $p < 0.05$ ,  $n = 3$ ). (c) SEM of alloy sample surface after 5 weeks of immersion in HBSS.

the ultimate tensile strength (UTS). The AZ31 alloy exhibits the highest UTS ( $260 \pm 7$  MPa), followed by LZ61 ( $179 \pm 3$  MPa), and LZ91 ( $146 \pm 8$  MPa), respectively.

Figure 2c, d shows the fracture surface of the tensile bars. All the samples experienced and displayed a similar cup-and-cone fracture morphology during the tensile test. The AZ31 alloy exhibited a mixture of both, ductile and brittle fracture. The major portion of the fracture surface shows an irregular and fibrous appearance, accompanied by several sharp and smooth cleavage planes which is indicative of a brittle fracture. The LZ61 and LZ91 alloys on the other hand, show much more necking before fracture (Figure 2c, d). Hence, only a predominantly ductile fracture pattern could be observed in the central interior region of the fracture surface. Higher-magnification SEM images (Figure 2d) further reveal that the fracture surface consisted of numerous spherical dimples. The dimpled feature is a typical structure that results from uniaxial tensile failure, and each dimple represents half of a microvoid that is formed, which then separates during the fracture process.

**3.3. In Vitro Degradation of Mg–Li–Zn Alloy.** Several techniques are commonly used to evaluate the degradation of magnesium alloys, such as electrochemical analysis, hydrogen evolution, and immersion tests. In this study, electrochemical and static immersion tests were conducted to study the degradation behavior of the Mg–Li–Zn alloys. Figure 3a shows the potentiodynamic polarization (PDP) curves collected for LZ61, LZ91, pure Mg and AZ31 alloy.  $E_{\text{corr}}$ ,  $i_{\text{corr}}$ , and  $\text{CR}_{\text{corr}}$  calculated based on the tafel plots are listed in Table 2. All the

**Table 2. Corrosion Rates of Pure Mg, AZ31, LZ61, and LZ91 Alloys Determined by Potentiodynamic Polarization<sup>a</sup>**

	$E_{\text{corr}}$ (V)	$i_{\text{corr}}$ ( $\mu\text{A}/\text{cm}^2$ )	$\text{CR}_{\text{corr}}$ (mm/year)
pure Mg	$-1.46 \pm 0.03$	$1.094 \pm 0.373$	$0.025 \pm 0.008$
AZ31	$-1.52 \pm 0.01$	$2.144 \pm 0.139$	$0.035 \pm 0.002$
LZ61	$-1.54 \pm 0.03$	$1.725 \pm 0.888$	$0.042 \pm 0.020$
LZ91	$-1.57 \pm 0.01$	$6.367 \pm 0.511$	$0.158 \pm 0.013$

<sup>a</sup> $E_{\text{corr}}$ , corrosion potential;  $i_{\text{corr}}$ , corrosion current density;  $\text{CR}_{\text{corr}}$ , corrosion rate calculated based on  $i_{\text{corr}}$ .

groups showed dramatic increase in corrosion current 200–300 mV above the  $E_{\text{corr}}$  indicating the film breakdown characteristic. The anodic processes of all the Mg–Li–Zn alloys were altered when compared to pure Mg and AZ31 alloy, which implies that the corrosion was largely controlled by the anodic reaction. The corrosion current representing the dissolution reaction of the alloy is noticeably higher, which increased the overall corrosion current density.

Immersion test was further conducted to evaluate the long-term in vitro degradation of Mg–Li–Zn alloy in HBSS. The weight loss of samples at the end of each time point was converted into the corrosion rate and plotted in Figure 3b. The slowest corrosion rate was observed for the AZ31 group at all 1, 3, and 5 weeks' time point. LZ91 alloy exhibited the highest corrosion rate throughout the 5-week long immersion test. LZ61 alloy on the other hand, showed a moderate corrosion resistance which was close to the corrosion resistance of pure Mg. The statistical analysis result revealed that there is no statistical difference between the 5-week corrosion rates of pure Mg, AZ31 alloy, and LZ61 alloy groups, and the LZ91 alloy group corroded at significantly higher rate ( $p < 0.05$ ) than all the other groups.

The average corrosion rate determined following immersion tests showed a similar trend among all the groups studied suggesting that the corrosion rates expectedly increase over the period of immersion, and the 5-week corrosion rate was the highest compared to the corrosion rate after 1 week and 3 weeks of immersion. However, the corrosion rate after 3 weeks of immersion was the slowest for pure Mg and AZ31 alloy while the slowest corrosion rate for LZ61 alloy and LZ91 alloy was observed after 1 week of immersion. Figure 3c shows the SEM image of the sample surface without the corrosion product after 5 weeks of immersion. The sample surface of LZ61, pure Mg and AZ31 showed only partially corroded region, but the LZ91 alloy surface showed much higher roughness indicating a higher corrosion rate likely caused by the larger content of Li, a more reactive metal than Mg. Localized corrosion was, however, observed on the surface of all the samples studied reflective of the higher reactivity of both Li and Mg. Localized corrosion would potentially lead to fracture of the stents, and suitable coating will therefore be needed to protect the stents from likely rapid loss of mechanical integrity of the stent.

**3.4. In Vitro Cytotoxicity of Mg–Li–Zn Alloy.** In vitro biocompatibility evaluation of Mg alloy is challenging since current ISO and ASTM standards are not applied to biodegradable metals. Efforts have therefore been made to standardize the in vitro cytotoxicity protocol for Mg alloys,<sup>37</sup> however no standard protocol has been established as yet. In the present study, four tests were designed to (1) measure the specific aspects of cellular metabolism (MTT assay); (2) assess the cell damage by imaging the cell morphology (live/dead imaging, DAPI&F-actin staining); (3) evaluate the cell damage (cell apoptosis assay); and finally, (4) measure the cell growth (cell cycle assay). All these tests were conducted in an indirect fashion using the alloy extracts.

The ICP result (Figure 4a, d) indicates a burst release of Mg and Li ions collected from pure Mg and Mg alloys after incubation for 72 h in the appropriate cell culture medium. The concentration of Zn was below the detection limits and hence, was not plotted. It can be seen that the Mg ion concentration increases more than 10-fold compared to normal cell culture medium for both SMCM and EBM-2 culture media. For SMCM, there was no significant difference in Mg ion concentration between LZ61 alloy and LZ91 alloy extract ( $p > 0.05$ ). The Mg concentration in both LZ61 alloy and LZ91 alloy extracts were significantly higher than normal SMCM but significantly lower than pure Mg and AZ31 alloy extract ( $p < 0.05$ ). Li ion concentration was also significantly higher in LZ91 alloy extract than LZ61 alloy extract ( $p < 0.05$ ). Similar trends applied to EBM-2, the only difference being that there was significant difference in Mg ion concentration between pure Mg and the AZ31 alloy extract ( $p < 0.05$ ).

HASMC viability was negatively correlated to extract concentration with higher cell viability in lower extract concentration. The cell viability in 75% extract after culturing for both 1 day and 3 days was less than 20%, and even close to 0% for the AZ31 alloy group. At day 1, only groups with extract concentration below 50% showed close to or more than 100% cell viability. At day 3, only the 10% extract group showed more than 100% cell viability. Two-way ANOVA was performed to analyze the statistical difference between the different alloy groups. Magnesium alloy group and extract dilution ratio served as the two independent variables and cell viability served as the dependent variables in the two-way ANOVA analysis. Cell

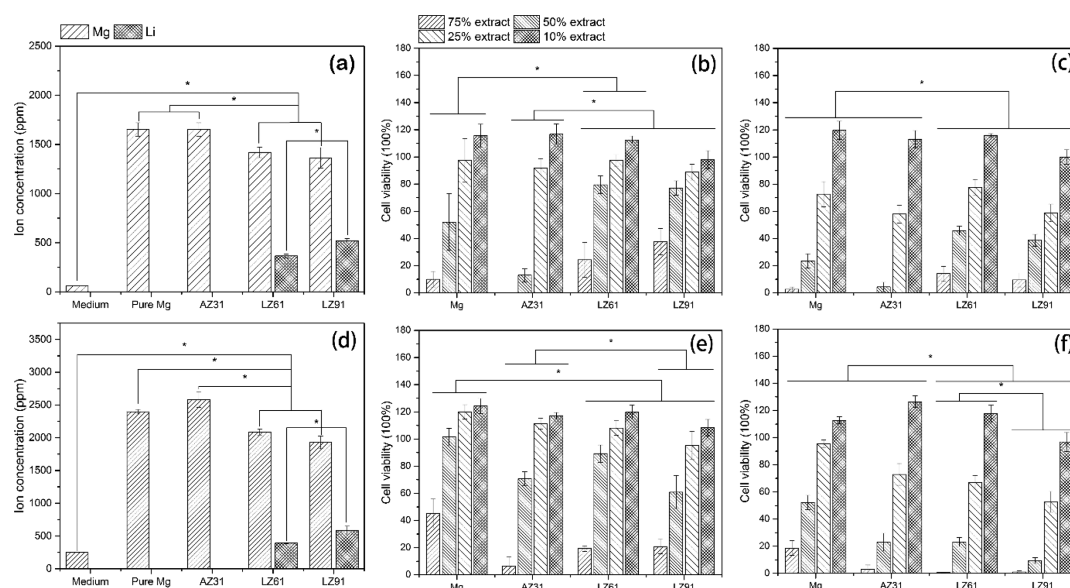


**Figure 4.** In vitro cytotoxicity of Mg–Li–Zn alloy. (a) Mg and Li ion concentration in SMCM medium and extract; (b) HASMC viability after culturing in different concentration extract for 1 day; (c) HASMC viability after culturing in different concentration extract for 3 days; (d) Mg and Li ion concentration in EBM-2 medium and extract; (e) HUVEC viability after culturing in different concentration extract for 1 day; (f) HUVEC viability after culturing in different concentration extract for 3 days; \*denotes a significant difference between alloy groups ( $p < 0.05$ ,  $n = 3$ ).

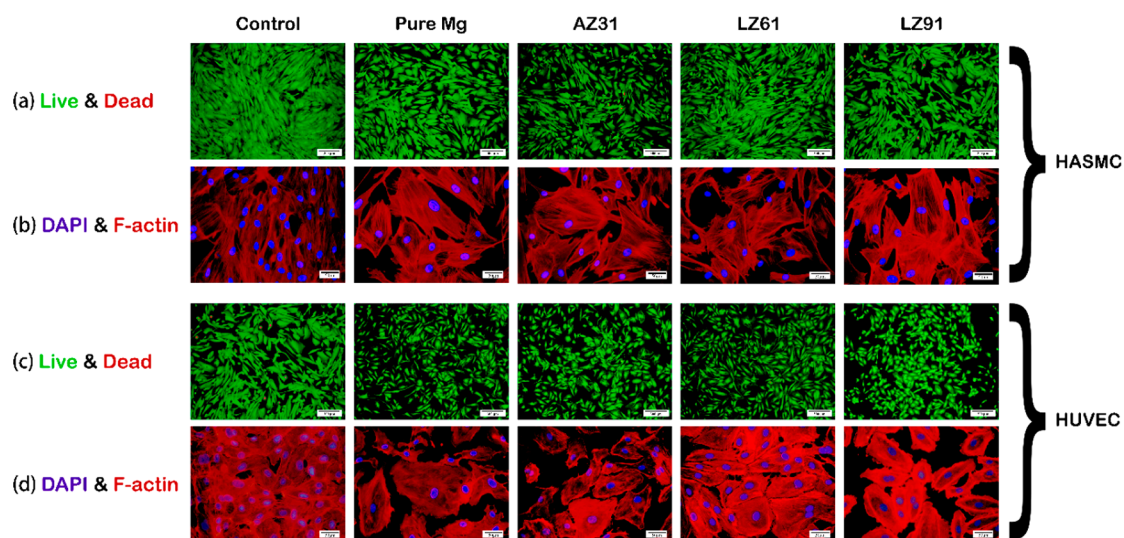


**Figure 5.** Live/dead staining of (a) HASMC, (c) HUVEC after 3 days culture in 25% extract or normal cell culture medium (control), scale bar = 300  $\mu\text{m}$ ; DAPI/F-actin staining of (b) HASMC, (d) HUVEC after 3 days culture in extract or normal cell culture medium (control), scale bar = 50  $\mu\text{m}$ .

viability of each magnesium alloy group is discussed as an independent variable in general regardless of the extract dilution ratio. At day 1, there is no significant difference observed between the LZ61 alloy group and the LZ91 alloy group ( $p > 0.05$ ). Both the LZ61 alloy and LZ91 groups showed higher cell viability than AZ31 group ( $p < 0.05$ ), which is because of the high cell viability at 75% extract dilution ratio. Only the LZ61 alloy group showed higher cell viability than the pure Mg group ( $p < 0.05$ ). There is no statistical difference between the LZ91 alloy group and the pure Mg group. At day 3, no significant difference was observed between LZ61 alloy group and LZ91 alloy group ( $p > 0.05$ ). Both LZ61 and LZ91 alloy groups, however, showed higher cell viability than pure Mg group ( $p < 0.05$ ) as well as the AZ31 alloy group ( $p < 0.05$ ).

Similar results were observed for the HUVEC cells. Higher HUVEC viability was observed in lower extract concentrations. At day 1, there is no statistically significant difference observed between LZ61 alloy group and LZ91 alloy group ( $p < 0.05$ ). Both LZ61 alloy and LZ91 groups showed lower cell viability than Mg group ( $p < 0.05$ ) and LZ91 alloy group, however, showed lower cell viability than AZ31 alloy group ( $p < 0.05$ ). There is also no statistical difference observed between the LZ61 alloy and AZ31 alloy group. At day 3 however, significant difference was observed between the LZ61 alloy group and LZ91 alloy group ( $p < 0.05$ ). Both LZ61 and LZ91 alloy groups showed lower cell viability than pure Mg group ( $p < 0.05$ ) as well as the AZ31 alloy group ( $p < 0.05$ ).

Based on MTT results, 25% extract was the only group that showed the impact of degradation products on the different

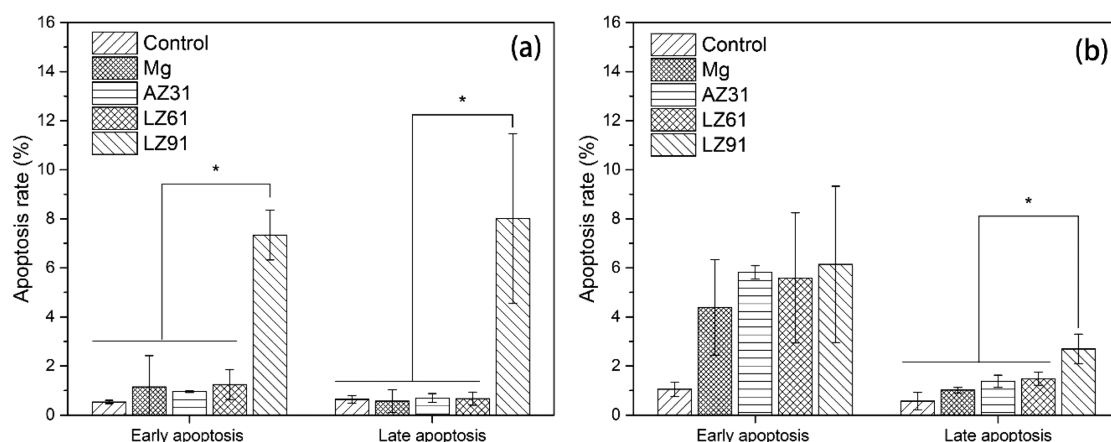


**Figure 6.** Early apoptosis and later apoptosis rate of (a) HASMC and (b) HUVEC after culturing in 25% extract for 24 h. \*denotes a significant difference between alloy groups ( $p < 0.05$ ,  $n = 3$ ).

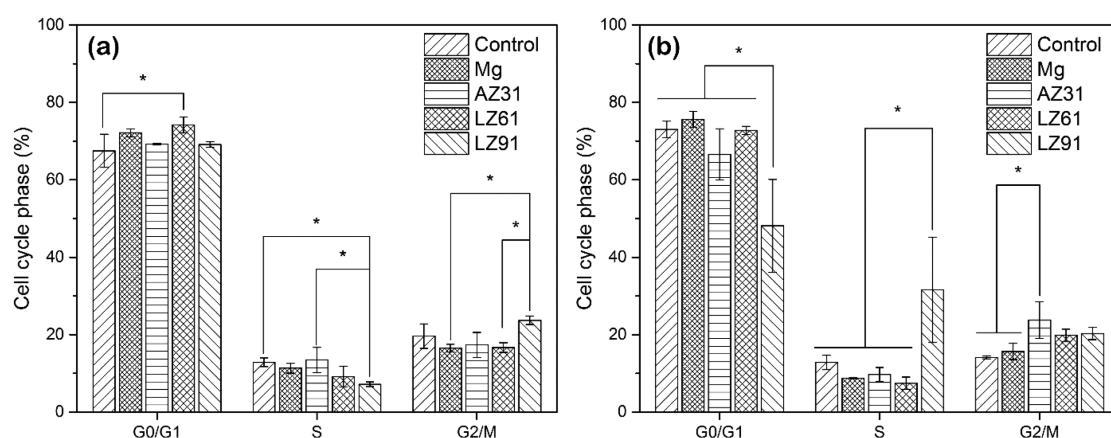


**Figure 7.** Percentage of cell in at different cell cycle phase after culturing in 25% extract for 24 h: (a) HASMC and (b) HUVEC. \*denotes a significant difference between alloy groups ( $p < 0.05$ ,  $n = 3$ ).

cells while still supporting limited cell proliferation. Therefore, 25% extract was used for live/dead staining and DAPI/F-actin staining to visualize the impact of the degradation products on cells. Despite the differences observed in the MTT assay discussed above, the live/dead staining of HASMC and HUVEC after culturing in 25% extract showed similar results (Figure 5(a, c)). All pure Mg and Mg alloy groups showed lower cell density when compared to the control group, wherein cells were cultured in normal cell culture medium. The LZ61 alloy and LZ91 alloy groups demonstrated comparable live cell density with very few apoptotic cells. Regardless of the lower cell density, all the pure Mg and Mg alloy groups showed same cell morphology as the cells cultured in normal cell culture medium (Figure 5(b, d)). The HASMCs demonstrated a spindle shaped cell morphology while the HUVECs exhibited a rather rounded shaped cell morphology.

The effect of degradation products on cell apoptosis and cell cycle were further investigated by culturing the cells in 25% extract for 24 h. The apoptosis assay demonstrate a significantly higher early apoptosis and late apoptosis of HASMC cells in the LZ91 alloy group when compared to the other alloy groups ( $p < 0.05$ ) (Figure 6a). For the HUVECs, the LZ91 alloy group exhibit significantly higher late stage apoptosis rate ( $p < 0.05$ ) compared to the other groups. For the LZ61 alloy group, the apoptosis rate did not show any significant difference when compared to the control, pure Mg and AZ31 alloy groups ( $p <$

0.05). As depicted in Figure 7(a), pure Mg and Mg alloy extract exhibit similar distribution of HASMC in each of the cell cycle phases to the control groups, where the cells were cultured in normal cell culture medium. However, for HUVEC, significantly less cells were observed for the LZ91 in the G0/G1 phase ( $p < 0.05$ ), whereas more cells were arrested for LZ91 in the S phase ( $p < 0.05$ ) with all metal groups showing similar percentage of cells in the G2/M phase (Figure 7b).

**3.5. In Vivo Degradation of Mg–Li–Zn Alloy in Mouse Subcutaneous Model.** The most clinically relevant animal model for studying biodegradation in a vascular environment is the porcine animal model.<sup>38–40</sup> Some study also reported using the rabbit abdominal aorta model.<sup>41</sup> Pierson et al. on the other hand, proposed a simplified in vivo model by implanting magnesium alloy wire into the rat abdominal aorta wall or the lumen to mimic the conditions of stent implantation.<sup>42</sup> However, these animal models are relatively complicated and less cost-efficient for early stage in vivo evaluation. Therefore, to obtain an initial in vivo assessment, the in vivo degradation behavior and biocompatibility of the Mg–Li–Zn alloys was studied herein in a simple mouse subcutaneous model. The release of  $H_2$ , weight loss, and size of the  $H_2$  bubbles released were measured to understand the degradation rate and also assess the accumulation of the degradation products of Mg–Li–Zn alloy.

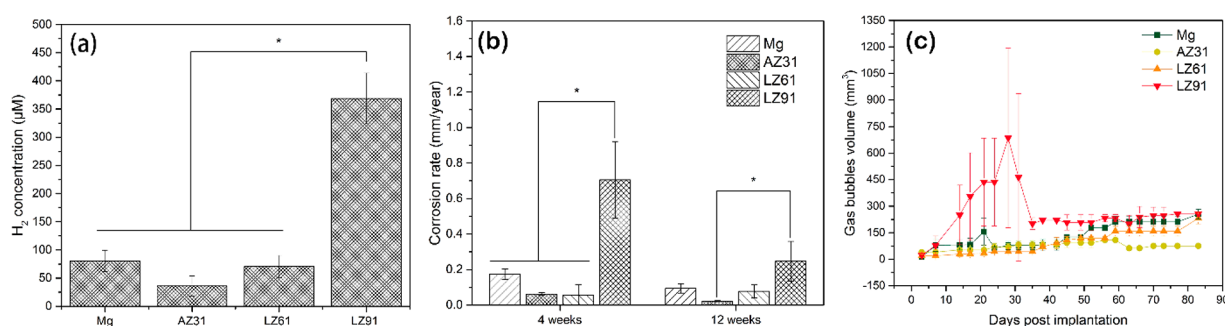


**Figure 8.** In vivo degradation rate of Mg–Li–Zn alloys in rat subcutaneous model. (a) H<sub>2</sub> concentration measured on anaesthetized nude mice with AZ31, pure Mg, LZ61, and LZ91 implanted subcutaneously 1 week after implantation; (b) sample weight loss after 4 weeks and 12 weeks of implantation; (c) size of H<sub>2</sub> gas bubbles generated during the 12-week implantation. \*denotes a significant difference between alloy groups ( $p < 0.05$ ,  $n = 3$ ).

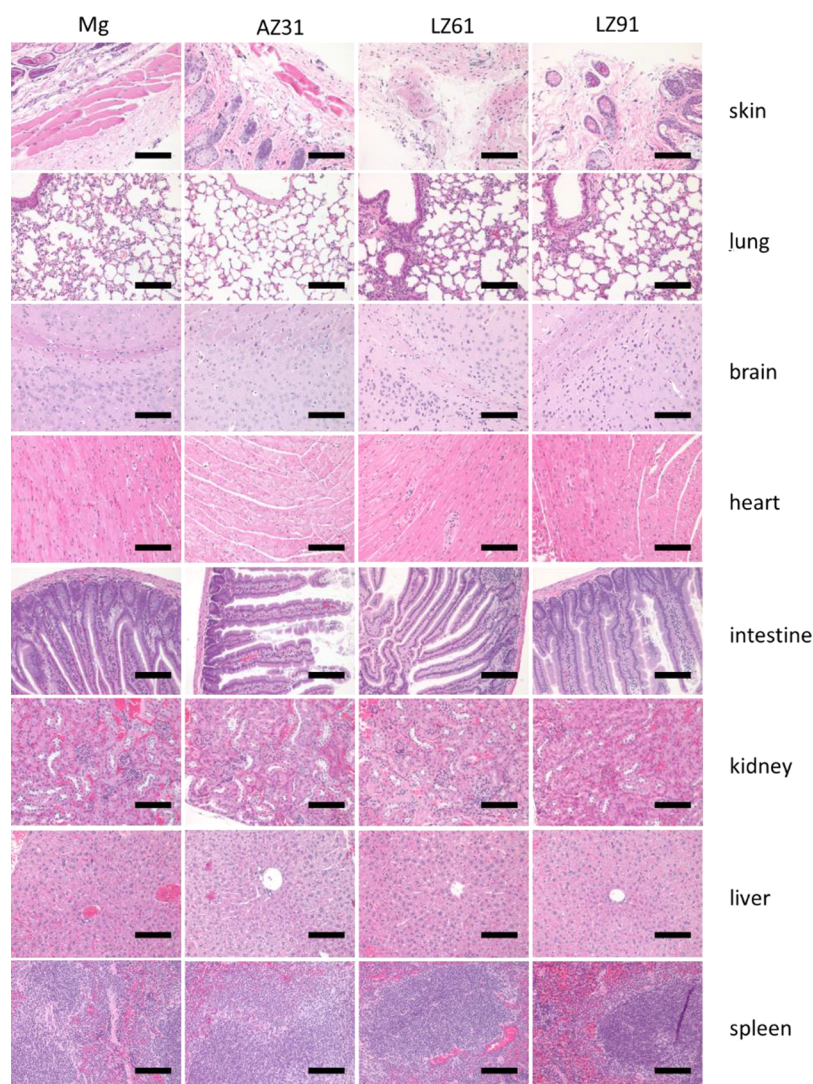


**Figure 9.** H&E staining of skin, lung, brain, heart, intestine, kidney, liver, and spleen after 12 weeks of implantation (scale bar = 0.25 mm).

Our earlier study showed that measurements of H<sub>2</sub> release from the biodegrading Mg implanted subcutaneously in mice obtained noninvasively by just pressing the tip of an amperometric H<sub>2</sub> sensor against the skin covering the implant were similar to those made invasively by inserting the sensor tip inside the cavity.<sup>33</sup> Subsequent research showed the effectiveness of the transdermal H<sub>2</sub> measurements in studying the Mg

alloys exhibiting different corrosion rates.<sup>32,34,43,44</sup> Herein therefore, we used the transdermal measurement of H<sub>2</sub> from four biodegradable alloys implanted subcutaneously in mice with the electrochemical H<sub>2</sub> sensor. The transdermal H<sub>2</sub> sensing was first explored using LZ91 alloy, which corrodes rapidly enough to create sufficient amounts of H<sub>2</sub> gas to form visible gas cavities. The H<sub>2</sub> microsensor tip was positioned

directly on the gas cavity that surrounds the implants to obtain each measurement. As shown in Figure 8a, the  $H_2$  concentration is  $368 \pm 45 \mu\text{M}$  for the LZ91 alloy after 1-week implantation. Similarly,  $H_2$  concentrations of  $70 \pm 20 \mu\text{M}$ ,  $80 \pm 18 \mu\text{M}$ , and  $36 \pm 18 \mu\text{M}$  were obtained for LZ61, pure Mg and AZ31 under the same condition, respectively. Error bars are standard deviation for measurement made on three mice ( $n = 3$ ). As expected, the higher corroding alloys produce more  $H_2$ . The  $H_2$  concentration at the center of the gas cavity is on the order of LZ91 > LZ61  $\approx$  pure Mg > AZ31, with LZ91 alloy group exhibiting significantly higher amounts of hydrogen release than all the other groups ( $p < 0.05$ ), which suggests that the LZ91 alloy exhibits the highest corrosion among all the alloys studied. The in vivo weight losses measured at 4 and 12 weeks were converted into in vivo corrosion rates and plotted in Figure 8b, which also showed the same order of corrosion proficiency as indicated by the  $H_2$  concentration measurements 1 week after implantation. Correspondingly, it can be concluded that the LZ91 alloy group corroded significantly faster than the rest of the groups after both 4 weeks and 12 weeks of implantation ( $p < 0.05$ ) reflective of the higher Li content as discussed earlier.

The formation of gas cavities is another concern of magnesium implants.<sup>45</sup> The main source of gas formation in Mg alloys is the degradation process of the magnesium implant depending on the metal composition and exposed surface area. In the subcutaneous model, Heineman and Witte have demonstrated that the gas cavities will slowly be absorbed by diffusing through the skin as well as the capillaries and transported through by the vascular system.<sup>46</sup> The sizes of the gas cavities were measured to qualitatively correlate and assess the biodegradation rate of all of these four alloys studied in vivo. As seen in Figure 8c, the volume of the gas cavity is largest for LZ91 at all the time points measured, which is consistent with the measurement of the  $H_2$  concentration (Figure 8a) and in vivo corrosion rate (Figure 8b). The gas cavity in the mice bearing LZ91 increases during the first 4 weeks and reaches a maximum size of  $685 \pm 507 \text{ mm}^3$  ( $n = 6$ ) by 4 weeks after implantation. In the case of LZ61 and pure Mg, the size of the gas cavity continually increased for 3 months. The size of the gas cavity for AZ31 continuously increased until 2 months after surgery, after which the size decreased until the end of the study. The size of the gas cavity for the AZ31 alloy is the smallest compared to LZ91, LZ61 and pure Mg which suggests that the biodegradation rate for AZ31 is the lowest among the groups studied herein. From the above analysis, the corrosion rate among the alloy groups can be considered to vary in the following order of LZ91 > LZ61  $\approx$  pure Mg > AZ31, which is consistent with the  $H_2$  and weight loss measurements. These analysis are in line with the in vitro corrosion studies outlined earlier. The higher Li content adds to the higher corrosion rate of the LZ91 alloy, whereas AZ31 shows a lower corrosion rate in agreement with the known influence of Al to increase the corrosion resistance.<sup>47,48</sup>

### 3.6. H&E Study of the Biodegradation of These Alloys.

Histology analysis were further conducted to assess the local toxicity and systemic toxicity of the metal itself, the degradation process, and the degradation products. The mice implanted with the LZ61, LZ91, pure Mg, and AZ31 alloys were accordingly sacrificed at 12 weeks following surgery. Eight organs (skin, lung, brain, heart, intestine, kidney, liver, and spleen) were prepared into the specific pathological sections and were stained with hematoxylin and eosin. The correspond-

ing histological images obtained are shown in Figure 9. The H&E stains shows that there is no apparent pathological alteration in any of the tissue obtained from the experimental animals (Figure 9). No significant macrophage infiltration was observed in the skin tissue surrounding the implant site indicating no inflammatory response to the implanted Mg–Li–Zn alloy as well as pure Mg and AZ31 alloys. Other major organs that are involved in the metabolic clearance of  $\text{Mg}^{2+}$  also did not exhibit any noticeable abnormality. The H&E staining image of the kidney tissue obtained in all the experimental groups show clear and healthy epithelial cell structure without exhibiting any signs of distortion or congestion as well as particle degeneration and necrosis. No infiltration of inflammatory cells is also observed. Liver sections also clearly show healthy hepatic lobule as well as uniform cytoplasm which are arranged in a normal pattern. Spleen sections also show clear red and white pulp without any capsule thickening and signs of possible inflammatory response. Other organs, namely lung, heart, brain, and intestine, were also studied with H&E staining as shown in Figure 9. The stained tissue samples clearly indicate no abnormality or any noticeable biocompatibility issues in all of the above organs analyzed attesting to the favorable biocompatibility response of the Mg–Li–Zn alloys considered in this study.

## 4. DISCUSSION

In the present study, we have demonstrated the promising potential of two different Mg–Li–Zn alloys considered for possible application as biodegradable stents in the vascular arena. By alloying with Li and Zn, we successfully produced LZ61 and LZ91 alloys. The coexistence of both,  $\alpha$  ( $\text{Li}_{0.92}\text{Mg}_{4.08}$ ) and  $\beta$  ( $\text{Li}_3\text{Mg}_7$ ) phases are verified by the optical micrographs of the corresponding dual-phase microstructure as well as the XRD patterns discussed earlier.

For stent application, as outlined earlier, the ductility of the alloy is one of the critical determining factors for evaluation of the alloy proficiency for use as stents. It is well-known that in polycrystalline magnesium alloy, which exhibits the hexagonal close packed (HCP) structure, the room-temperature ductility is limited because of the lack of allowable slip systems. The dominant slip mode for magnesium has the burger vector  $1/3 \langle 11\bar{2}1 \rangle$  with the basal plane serving as the primary slip plane.<sup>49</sup> However, by creating the alloys with the introduction of Li and Zn considered in the present study, the tensile test successfully demonstrates that the ductility of the magnesium alloy is significantly improved by introducing the body centered cubic (BCC) phase into the Mg–Li alloy by effectively alloying with Li. However, a decrease in the tensile strength is also overserved because of the softer nature of the Li metal. Lee et al. reported that adding 1.2 wt % of Li would increase the strength of the Mg alloys because of solid solution strengthening. However, with more Li additions (>4.2 wt %), the strength and strain hardening rate decreased.<sup>50</sup> These results are clearly in line with the current study. This phenomenon could be explained to be attributable to the following: (1) In the  $\alpha$  phase, the critically resolved shear stress (CRSS) is decreased with the presence of Li, which leads to the activation of the nonbasal slip.<sup>51</sup> Lower critically resolved shear stress enables plastic deformation of Mg–Li–Zn alloy to occur at lower applied force which thus, results in lower yield strengths (YS) and ultimate tensile strengths (UTS). The activation of the nonbasal slip, however, further enhances the ductility of the Mg–Li–Zn alloy. (2) With the presence of the

BCC structure, the  $\beta$  phase of Mg–Li–Zn alloy provides more slip systems than the  $-\alpha$  phase, which as mentioned above exhibits the HCP structure. The  $\beta$  phase is relatively softer than the  $-\alpha$  phase, which leads to decrease in the strength and improves the ductility of Mg–Li–Zn alloy. (3) Alloying of Li also alters the lattice parameter of the magnesium crystal. Hardie and Parkins studied the lattice distortion of a series of binary magnesium alloy solutions and discovered that the addition of Li decreases both  $a$  and  $c$  lattice parameter spacing, particularly, the  $c$  lattice parameter spacing.<sup>52</sup> This lattice distortion caused by Li is believed to ease the cross gliding of the nonbasal slip contributing to enhanced ductility. It should be mentioned that it is possible that control of the second phase precipitates and microstructure control of the size and volume fraction could lead to improvements in the strength without compromising the biocompatibility and corrosion. These aspects, however, were not considered in the present study, as the primary aim was to demonstrate the higher ductility by alloying with Li and Zn.

The alloyed system of Mg–Li–Zn is expected to be more susceptible to corrosion because Li is a very active and reactive element. However, it is surprising to see that the LZ61 alloy exhibited no significant difference when compared to pure Mg and AZ31 after 5 weeks of immersion in HBSS. The corrosion resistance of Mg alloys is known to be mainly influenced by the presence of a protective oxide film on the alloy surface. It is also observed in the immersion study that both, the LZ61 and LZ91 alloys generated more fine hydrogen bubbles right after the samples were immersed into HBSS. The bubbles then grow larger and more stable as the sample surface loses its metallic sheen and luster. As shown in Figure 3, the 5-week corrosion rate of LZ61 and LZ91 is much less than the  $CR_{\text{corr}}$ , the corrosion rate calculated from  $i_{\text{corr}}$  (Table 2). The  $CR_{\text{corr}}$  depicted in Table 2 represents the corrosion tendency of the fresh alloy surface, whereas the 5-week corrosion rate calculated from the immersion test is the average corrosion rate determined over a long period of immersion. This result therefore implies that the bare Mg–Li–Zn alloy surface itself is prone to corrosion and therefore, showed a higher  $CR_{\text{corr}}$ , but the corrosion rate will be significantly lowered after the protective film is typically formed on the alloy surface. The decreasing corrosion rate is likely due to the formation of an increasingly thick corrosion layer of  $Mg(OH)_2$ ,  $MgCO_3$  and  $Mg_3(PO_4)_2$  products that coat the implant surface.<sup>33</sup> Song et al. reported that, for the dual phase Mg–Li alloys, the initial corrosion commenced at the interface of the  $\alpha$  phase and the  $\beta$  phase followed by spreading across the entire sample surface.<sup>53</sup>

As the corrosion continued, the oxide film on the surface of the Mg–Li–Zn alloy became thicker, consequently, providing more corrosion protection. However, the thicker the protective film, the more the brittle nature of the ceramic oxide formed which would lead to a higher propensity of crack formation. The integrity of the protective film is, however, determined by two major factors: pH value of the medium and the  $Cl^-$  ion concentration. Higher pH value will help stabilize the protective film, whereas a higher  $Cl^-$  concentration is detrimental to the integrity of the film. Because of the large volume of the HBSS solution and its buffering capacity, the pH value of the medium remained neutral over the duration of immersion. The  $Cl^-$  in HBSS penetrated the protective film thus resulting in crack formation. Further subsequent corrosion of Mg–Li–Zn alloy is localized in the area wherein the alloy is unprotected. Our study thus clearly demonstrates that the LZ91 alloy corrodes the

fastest among all the tested groups while the LZ61 alloy corroded much slower. Since there is a higher percentage of the  $\beta$  phase with a higher amount of Li in the Mg–Li–Zn alloy of LZ91, and the  $\beta$  phase is more active than the  $\alpha$  phase in aqueous environment, it is possible that the protective film on the surface of the  $\beta$  phase is less stable and provides less corrosion protection which causes the difference in the measured and observed corrosion resistance between the LZ61 alloy and LZ91 alloys. Figure 10 also summarizes the

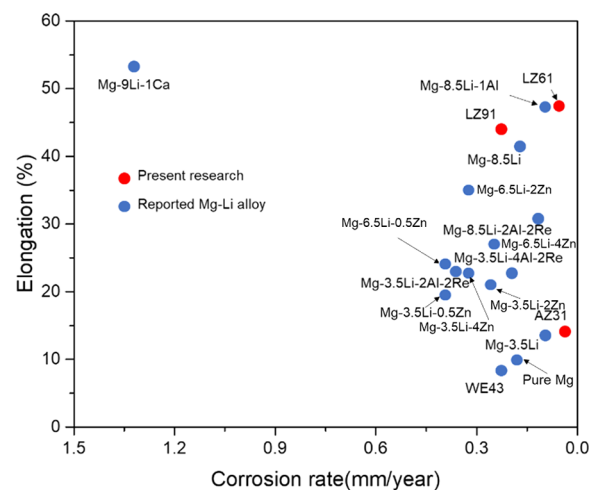


Figure 10. Summary of elongation and corrosion rate of reported Mg–Li alloys.<sup>21,22,27,57</sup>

degradation rate in simulated physiological buffer and the elongation to fracture of current Mg–Li alloys that has been reported for biomedical application. In comparison, it can be seen that the LZ61 alloy reported herein shows the excellent balance of corrosion rate and ductility. Even though Mg-8.5Li-1Al as reported in the literature showed similar low corrosion rate and ductility, it should be noted that LZ61 is free of Al, an element that has been extensively reported to be affiliated with causing damage to the nervous systems.<sup>54–56</sup>

Smooth muscle cells and endothelial cells are the two reverent cells that will interact with the magnesium stents following implantation. Therefore, the two human prime cells, HASMC and HUVEC, were selected for evaluating the in vitro cytotoxicity of the two selected Mg–Li–Zn alloys of LZ61 and LZ91, respectively. Previous study<sup>31</sup> showed that vascular cells exhibited low viability when directly seeded on Mg alloy surface. Therefore, in this study, all cytotoxicity tests were conducted in an indirect manner using the extract protocol. We first prepared extract following EN ISO standard 10993–12:2004 and investigated the ion concentrations in the extract, since the ion concentration is positively correlated to the pH value and osmolality.<sup>58</sup> The degradation of Mg alloy indeed led to a burst release of metal ions. However, when the Mg alloy is implanted in vivo, the surrounding physiological environment provides a barrier against the dramatic release of ions. To better mimic the in vivo environment, we further diluted the extract into four different concentrations in the MTT assay. Correspondingly, the indirect MTT assay results indicated that 75 and 50% extract concentration resulted in relatively lower cell viability especially after 3 days, whereas the 10% extract promoted the cell viability. Therefore, the 25% extracts were selected as the extract concentration for all the other in vitro cyto-compatibility tests conducted in this study.

The accumulation of degradation product in the extract led to an increase in the apoptosis rate in both HASCMs and HUVECs. Even though LZ91 alloy groups showed a significant increase in the apoptosis rate, we do notice that the average apoptosis rate is higher for all the pure Mg group and Mg alloy groups than the negative control group. This result is in agreement with previous studies, where Mg alloy extract caused an increase in the cell apoptosis rate.<sup>41,59,60</sup> Zhanhui Wang et al. believe that the elevated pH value, and Mg ion concentration are the determining factors that contribute to the observed cell apoptosis.<sup>59</sup> The increase in apoptosis rate also explains why the cell viability is lower at day 3 in the MTT assay for all the extract concentrations studied except for the 10% extract. The effect of extract on the cell cycle also depends on the cell types.

Zhanhui Wang et al. reported that more intestinal epithelial cells were locked in the G1/G0 phase but less cells were present in the S phase. In this study, the cell cycle phase distribution of HASMC cells were by and large observed to be similar, with certain groups exhibiting slightly higher than other groups. For HUVEC cells on the other hand, the extract of LZ91 arrest more cells in the S phase. On the basis of the results from this study and previous studies, it could be concluded that the degradation product might affect the occurrence and progression of all the three phases of cell proliferation and the effect will depend on the alloy composition and corrosion rate. Despite these effects discussed above, the cell morphology of HASMC and HUVEC remained normal after culturing for 3 days in 25% extract, which indicates that the surviving cells might still function well. The effect of Li ion on the HASMC and HUVEC is not clear, because the effect of the extract is indeed a combination of all alloying elements. Wang et al. proved that LiCl inhibits vascular smooth muscle cells proliferation and migration.<sup>61</sup> However, in the present study, the extract of LZ61 and LZ91 alloys did not reduce the cell viability of HASMC and HUVEC as well as the cell apoptosis rate and the cell cycle stages. Further study is required to clearly understand the effect of Li ion on both the HASMC and HUVEC cell response and eventual fate.

The corrosion rates of LZ61 and LZ91 reported herein are nevertheless, consistent throughout the in vitro and in vivo studies with LZ91 showing significantly higher corrosion than all the other groups, and LZ61 showing no significant difference compared to pure Mg and AZ31 alloy groups studied. The corrosion rate in vivo reduced significantly after 4-week of implantation, which led to the low average corrosion rate at week 12 and the smaller size of the gas cavities. Previous studies reported have shown that the in vivo and in vitro corrosion rates of Mg alloys tend to be conflicted with the results sometimes being totally different or even opposite,<sup>62,63</sup> drawing in general more favorable attention to in vivo results and assessment in contrast to in vitro analyses and believing the ensuing conclusions. The consistent corrosion rates of Mg–Li–Zn alloys (LZ61 and LZ91) obtained and observed in the present study conducted herein might imply that the corrosion mechanism is less prone to be susceptible to the surrounding environment, and the alloy probably goes through similar corrosion mechanisms under both in vitro and in vivo conditions. More detailed studies conducted likely in a dynamic bioreactor environment would likely be necessary to understand the similar responses seen in the current study. Such a study will likely be conducted in the near future.

Our H&E analysis also showed that there were no substantial signs of necrosis, expansion, inflammation, swelling, encapsu-

lation, hemorrhage, or any perceived discoloration of the key organs nor at the implant site. The histological analyses also indicate that addition of Li element into these alloys and their varying corrosion rate did not introduce any semblance of encapsulation, toxicity, necrosis, hemorrhage, discoloration, or excessive inflammatory response to the surrounding tissue. These results taken in total indicate that the LZ61, LZ91, pure Mg, and AZ31 alloys studied here all showed good biocompatibility when assessed in the 8 animal organs harvested at the end of the 3 months. It can be safely inferred based on the results reported herein that the alloys implanted in the animals at the early stage can be indeed considered to be biologically safe and the experimental animals tolerated the degradation products generated by these alloys. Similarly, previous study also demonstrated that no biocompatibility issue was caused by AZ31 after 2 months implantation under similar conditions.<sup>64</sup> The current assessment thus elucidates the potential of the new class of ultrahigh ductility alloys for possible applications requiring high plastic deformation such as in a variety of stent applications. Subsequent ongoing work to be reported in future publications will further demonstrate the efficacy of this system for in vivo stent applications.

## 5. CONCLUSIONS

Two multiphase Mg–Li–Zn alloys, LZ61 and LZ91, were fabricated and evaluated for both in vitro and in vivo stent application. This difference in the alloy microstructure clearly results in the observed difference in mechanical properties (yield strength (YS), ultimate tensile strength (UTS), and elongation at fracture), degradation, and cytotoxicity. The major conclusions of this study are as follows:

- (1) Both LZ61 and LZ91 alloy showed significant improvements in ductility, reaching more than 40% elongation at fracture. The strength of both alloys decreased when compared to AZ31 alloy. With a higher percentage of the  $\beta$  phase in the LZ91 alloys, the alloy therefore exhibited lower YS and UTS than LZ61 alloy. The improvement in ductility will facilitate favorable processing of the material allowing for stent design, and appropriate manufacturing of the stent.
- (2) The Mg–Li–Zn alloys (LZ61 and LZ91) however, showed consistent degradation rates both in vitro and in vivo. Particularly, for LZ61, the corrosion rate showed nonsignificant difference compared to the corrosion rates of pure Mg and AZ31. Correspondingly, it can be construed that the LZ61 alloys are likely more suitable for cardiovascular stent application which requires a relatively slower corrosion providing longer support from the stents. The LZ91 alloys, on the other hand, might be more suitable for other stent applications that do not require the long-term presence of the implanted device.
- (3) Both Mg–Li–Zn alloys (LZ61 and LZ91) showed comparable in vitro cytotoxicity with no noticeable local and systematic in vivo toxicity. Particularly, for the LZ61 alloy, similar results of cell viability, cell apoptosis, and proliferation to pure Mg and AZ31 alloy were observed. Histological assessment also shows that both Mg–Li–Zn alloys (LZ61 and LZ91) do not introduce any toxic response in the various organs studied, even for the very rapidly corroding LZ91 alloy, which would subject the organs to the highest concentration of soluble products.

In summary, this study clearly indicates that the multiphase ultrahigh ductility Mg–Li–Zn alloys displays the potential to be not only fabricated but also likely deployed in *in vivo* studies to validate their efficacy for stent application. Compared to LZ91, the LZ61 alloy showed better balance of mechanical properties, corrosion resistance and biocompatibility making them likely candidates for possible application as stents in cardiovascular as well as other application requiring the high ductility characteristics. Further studies will focus on optimizing the composition and processing of the LZ61 alloy combined with evaluation of the LZ61 prototype stent to be used in a clinically relevant animal model. These studies are currently being planned, the results of which will be discussed in future publications to follow shortly.

## AUTHOR INFORMATION

### Corresponding Author

\*E-mail: [pkumta@pitt.edu](mailto:pkumta@pitt.edu). Tel.: +1-412-648-0223. Fax: +1-412-624-3699.

### ORCID

Prashant N. Kumta: 0000-0003-1227-1249

### Notes

The authors declare no competing financial interest.

## ACKNOWLEDGMENTS

The authors gratefully acknowledge the support of the NSF funded Engineering Research Center–Revolutionizing Metallic Biomaterials (NSF-ERC-RMB) through grant-EEC-0812348. P.N.K. acknowledges the financial support of the National Science Foundation (CBET-0933153), Edward R. Weidlein Chair Professorship Funds, and the Center for Complex Engineered Multifunctional Materials (CCEMM), Swanson School of Engineering at the University of Pittsburgh for partial support of this research.

## REFERENCES

- (1) Xin, Y. C.; Liu, C. L.; Zhang, X. M.; Tang, G. Y.; Tian, X. B.; Chu, P. K. Corrosion behavior of biomedical AZ91 magnesium alloy in simulated body fluids. *J. Mater. Res.* **2007**, *22* (7), 2004–2011.
- (2) Yan, T. T.; Tan, L. L.; Xiong, D. S.; Liu, X. J.; Zhang, B. C.; Yang, K. Fluoride treatment and *in vitro* corrosion behavior of an AZ31B magnesium alloy. *Mater. Sci. Eng., C* **2010**, *30* (5), 740–748.
- (3) Willbold, E.; Kaya, A. A.; Kaya, R. A.; Beckmann, F.; Witte, F. Corrosion of magnesium alloy AZ31 screws is dependent on the implantation site. *Mater. Sci. Eng., B* **2011**, *176* (20), 1835–1840.
- (4) Qin, H.; Zhao, Y.; An, Z.; Cheng, M.; Wang, Q.; Cheng, T.; Wang, Q.; Wang, J.; Jiang, Y.; Zhang, X.; Yuan, G. Enhanced antibacterial properties, biocompatibility, and corrosion resistance of degradable Mg–Nd–Zn–Zr alloy. *Biomaterials* **2015**, *53* (0), 211–220.
- (5) Grunewald, T. A.; Ogier, A.; Akbarzadeh, J.; Meischel, M.; Peterlik, H.; Stanzl-Tschegg, S.; Löffler, J. F.; Weinberg, A. M.; Lichtenegger, H. C. Reaction of bone nanostructure to a biodegrading Magnesium WZ21 implant - A scanning small-angle X-ray scattering time study. *Acta Biomater.* **2016**, *31*, 448–457.
- (6) Guan, X.; Xiong, M.; Zeng, F.; Xu, B.; Yang, L.; Guo, H.; Niu, J.; Zhang, J.; Chen, C.; Pei, J.; Huang, H.; Yuan, G. Enhancement of osteogenesis and biodegradation control by brushite coating on Mg–Nd–Zn–Zr alloy for mandibular bone repair. *ACS Appl. Mater. Interfaces* **2014**, *6* (23), 21525–21533.
- (7) Chou, D. T.; Hong, D.; Saha, P.; Ferrero, J.; Lee, B.; Tan, Z.; Dong, Z.; Kumta, P. N. *In vitro* and *in vivo* corrosion, cytocompatibility and mechanical properties of biodegradable Mg–Y–Ca–Zr alloys as implant materials. *Acta Biomater.* **2013**, *9* (10), 8518–8533.

(8) Sandlöbes, S.; Friák, M.; Korte-Kerzel, S.; Pei, Z.; Neugebauer, J.; Raabe, D. A rare-earth free magnesium alloy with improved intrinsic ductility. *Sci. Rep.* **2017**, *7* (1), 10458.

(9) Bian, D.; Zhou, W.; Liu, Y.; Li, N.; Zheng, Y.; Sun, Z. Fatigue behaviors of HP-Mg, Mg–Ca and Mg–Zn–Ca biodegradable metals in air and simulated body fluid. *Acta Biomater.* **2016**, *41*, 351–60.

(10) Roland, T.; Reintant, D.; Lu, K.; Lu, J. Fatigue life improvement through surface nanostructuring of stainless steel by means of surface mechanical attrition treatment. *Ser. Mater.* **2006**, *54* (11), 1949–1954.

(11) Hanada, K.; Matsuzaki, K.; Huang, X.; Chino, Y. Fabrication of Mg alloy tubes for biodegradable stent application. *Mater. Sci. Eng., C* **2013**, *33* (8), 4746–4750.

(12) Zhang, Y.; Kent, D.; Wang, G.; StJohn, D.; Dargusch, M. S. The cold-rolling behaviour of AZ31 tubes for fabrication of biodegradable stents. *J. Mech. Behav. Biomed. Mater.* **2014**, *39* (0), 292–303.

(13) Wang, L.; Fang, G.; Qian, L.; Leeftang, S.; Duszczyk, J.; Zhou, J. Forming of magnesium alloy microtubes in the fabrication of biodegradable stents. *Prog. Nat. Sci.* **2014**, *24* (5), 500–506.

(14) Byrer, T. G.; Frost, P. D.; White, E. L.; Battelle Memorial, L.; United, S. *The Development of Magnesium-Lithium Alloys for Structural Applications*; National Aeronautics and Space Administration: Washington, D.C., 1964; p 34, A36, B40.

(15) Angrisani, N.; Reifennath, J.; Zimmermann, F.; Eifler, R.; Meyer-Lindenberg, A.; Vano-Herrera, K.; Vogt, C. Biocompatibility and degradation of LAE442-based magnesium alloys after implantation of up to 3.5 years in a rabbit model. *Acta Biomater.* **2016**, *44*, 355–365.

(16) Ullmann, B.; Reifennath, J.; Seitz, J. M.; Bormann, D.; Meyer-Lindenberg, A. Influence of the grain size on the *in vivo* degradation behaviour of the magnesium alloy LAE442. *Proc. Inst. Mech. Eng., Part H* **2013**, *227* (3), 317–326.

(17) Witte, F.; Fischer, J.; Nellesen, J.; Vogt, C.; Vogt, J.; Donath, T.; Beckmann, F. *In vivo* corrosion and corrosion protection of magnesium alloy LAE442. *Acta Biomater.* **2010**, *6* (5), 1792–1799.

(18) Nene, S. S.; Kashyap, B. P.; Prabhu, N.; Estrin, Y.; Al-Samman, T. Biocorrosion and biodegradation behavior of ultralight Mg–4Li–1Ca (LC41) alloy in simulated body fluid for degradable implant applications. *J. Mater. Sci.* **2015**, *50* (8), 3041–3050.

(19) Zeng, R. C.; Qi, W. C.; Zhang, F.; Cui, H. Z.; Zheng, Y. F. *In vitro* corrosion of Mg–1.21Li–1.12Ca–1Y alloy. *Prog. Nat. Sci.* **2014**, *24* (5), 492–499.

(20) Leeftang, M. A.; Dzwonczyk, J. S.; Zhou, J.; Duszczyk, J. Long-term biodegradation and associated hydrogen evolution of duplex-structured Mg–Li–Al–(RE) alloys and their mechanical properties. *Mater. Sci. Eng., B* **2011**, *176* (20), 1741–1745.

(21) Zhou, W. R.; Zheng, Y. F.; Leeftang, M. A.; Zhou, J. Mechanical property, biocorrosion and *in vitro* biocompatibility evaluations of Mg–Li–(Al)–(RE) alloys for future cardiovascular stent application. *Acta Biomater.* **2013**, *9* (10), 8488–8498.

(22) Zeng, R. C.; Sun, L.; Zheng, Y. F.; Cui, H. Z.; Han, E. H. Corrosion and characterisation of dual phase Mg–Li–Ca alloy in Hank's solution: The influence of microstructural features. *Corros. Sci.* **2014**, *79* (0), 69–82.

(23) Liu, X. H.; Du, G. J.; Wu, R. Z.; Niu, Z. Y.; Zhang, M. L. Deformation and microstructure evolution of a high strain rate superplastic Mg–Li–Zn alloy. *J. Alloys Compd.* **2011**, *509* (39), 9558–9561.

(24) Liu, X. H.; Zhan, H. B.; Gu, S. H.; Qu, Z. K.; Wu, R. Z.; Zhang, M. L. Superplasticity in a two-phase Mg–8Li–2Zn alloy processed by two-pass extrusion. *Mater. Sci. Eng., A* **2011**, *528* (19–20), 6157–6162.

(25) Takuda, H.; Matsusaka, H.; Kikuchi, S.; Kubota, K. Tensile properties of a few Mg–Li–Zn alloy thin sheets. *J. Mater. Sci.* **2002**, *37* (1), 51–57.

(26) Lin, Y. N.; Wu, H. Y.; Zhou, G. Z.; Chiu, C. H.; Lee, S. Mechanical and anisotropic behaviors of Mg–Li–Zn alloy thin sheets. *Mater. Eng.* **2008**, *29* (10), 2061–2065.

(27) Liu, Y.; Wu, Y.; Bian, D.; Gao, S.; Leeftang, S.; Guo, H.; Zheng, Y.; Zhou, J. Study on the Mg–Li–Zn ternary alloy system with improved

mechanical properties, good degradation performance and different responses to cells. *Acta Biomater.* **2017**, *62* (Suppl C), 418–433.

(28) Velikokhatnyi, O. I.; Kumta, P. N. First principles study of the elastic properties of magnesium and iron based bio-resorbable alloys. *Mater. Sci. Eng., B* **2018**, *230*, 20–23.

(29) Hong, D.; Saha, P.; Chou, D. T.; Lee, B.; Collins, B. E.; Tan, Z.; Dong, Z.; Kumta, P. N. In vitro degradation and cytotoxicity response of Mg-4% Zn-0.5% Zr (ZK40) alloy as a potential biodegradable material. *Acta Biomater.* **2013**, *9* (10), 8534–8547.

(30) Jang, Y.; Tan, Z.; Jurey, C.; Xu, Z.; Dong, Z.; Collins, B.; Yun, Y.; Sankar, J. Understanding corrosion behavior of Mg-Zn-Ca alloys from subcutaneous mouse model: effect of Zn element concentration and plasma electrolytic oxidation. *Mater. Sci. Eng., C* **2015**, *48*, 28–40.

(31) Tomayko, M. M.; Reynolds, C. P. Determination of subcutaneous tumor size in athymic (nude) mice. *Cancer Chemother. Pharmacol.* **1989**, *24* (3), 148–154.

(32) Zhao, D.; Wang, T.; Guo, X.; Kuhlmann, J.; Doepke, A.; Dong, Z.; Shanov, V. N.; Heineman, W. R. Monitoring biodegradation of magnesium implants with sensors. *JOM* **2016**, *68* (4), 1204–1208.

(33) Kuhlmann, J.; Bartsch, I.; Willbold, E.; Schuchardt, S.; Holz, O.; Hort, N.; Hoche, D.; Heineman, W. R.; Witte, F. Fast escape of hydrogen from gas cavities around corroding magnesium implants. *Acta Biomater.* **2013**, *9* (10), 8714–8721.

(34) Zhao, D.; Wang, T.; Kuhlmann, J.; Dong, Z.; Chen, S.; Joshi, M.; Salunke, P.; Shanov, V. N.; Hong, D.; Kumta, P. N.; Heineman, W. R. In vivo monitoring the biodegradation of magnesium alloys with an electrochemical H<sub>2</sub> sensor. *Acta Biomater.* **2016**, *36*, 361–368.

(35) Hermawan, H.; Dube, D.; Mantovani, D. Degradable metallic biomaterials: design and development of Fe-Mn alloys for stents. *J. Biomed. Mater. Res., Part A* **2010**, *93* (1), 1–11.

(36) Wang, B.; Guan, S. K.; Wang, J.; Wang, L. G.; Zhu, S. J. Effects of Nd on microstructures and properties of extruded Mg-2Zn-0.46Y-xNd alloys for stent application. *Mater. Sci. Eng., B* **2011**, *176* (20), 1673–1678.

(37) Wang, J.; Witte, F.; Xi, T.; Zheng, Y.; Yang, K.; Yang, Y.; Zhao, D.; Meng, J.; Li, Y.; Li, W.; Chan, K.; Qin, L. Recommendation for modifying current cytotoxicity testing standards for biodegradable magnesium-based materials. *Acta Biomater.* **2015**, *21* (0), 237–249.

(38) Waksman, R.; Pakala, R.; Kuchulakanti, P. K.; Baffour, R.; Hellinga, D.; Seabron, R.; Tio, F. O.; Wittchow, E.; Hartwig, S.; Harder, C.; Rohde, R.; Heublein, B.; Andreae, A.; Waldmann, K. H.; Haverich, A. Safety and efficacy of bioabsorbable magnesium alloy stents in porcine coronary arteries. *Catheter. Cardiovasc. Interv.* **2006**, *68* (4), 607–619.

(39) Pinto Slottow, T. L.; Pakala, R.; Waksman, R. Serial imaging and histology illustrating the degradation of a bioabsorbable magnesium stent in a porcine coronary artery. *Eur. Heart J.* **2008**, *29* (3), 314.

(40) Wittchow, E.; Adden, N.; Riedmuller, J.; Savard, C.; Waksman, R.; Braune, M. Bioresorbable drug-eluting magnesium-alloy scaffold: design and feasibility in a porcine coronary model. *EuroIntervention* **2013**, *8* (12), 1441–1450.

(41) Mao, L.; Shen, L.; Niu, J.; Zhang, J.; Ding, W.; Wu, Y.; Fan, R.; Yuan, G. Nanophasic biodegradation enhances the durability and biocompatibility of magnesium alloys for the next-generation vascular stents. *Nanoscale* **2013**, *5* (20), 9517–9522.

(42) Pierson, D.; Edick, J.; Tauscher, A.; Pokorney, E.; Bowen, P.; Gelbaugh, J.; Stinson, J.; Getty, H.; Lee, C. H.; Drelich, J.; Goldman, J. A simplified in vivo approach for evaluating the bioabsorbable behavior of candidate stent materials. *J. Biomed. Mater. Res., Part B* **2012**, *100* (1), 58–67.

(43) Zhao, D.; Wang, T.; Heineman, W. R. Advances in H<sub>2</sub> sensors for bioanalytical applications. *TrAC, Trends Anal. Chem.* **2016**, *79*, 269–275.

(44) Zhao, D.; Wang, T.; Hoagland, B.; Benson, D.; Dong, Z.; Chen, S.; Chou, D.; Hong, D.; Wu, J.; Kumta, P. N.; Heineman, W. R. Visual H<sub>2</sub> sensor for monitoring biodegradation of magnesium implants in vivo. *Acta Biomater.* **2016**, *45*, 399–409.

(45) Noviana, D.; Paramitha, D.; Ulum, M. F.; Hermawan, H. The effect of hydrogen gas evolution of magnesium implant on the

postimplantation mortality of rats. *J. Orthop. Transl.* **2016**, *5* (Suppl C), 9–15.

(46) Kuhlmann, J.; Bartsch, I.; Willbold, E.; Schuchardt, S.; Holz, O.; Hort, N.; Hoeche, D.; Heineman, W. R.; Witte, F. Fast escape of hydrogen from gas cavities around corroding magnesium implants. *Acta Biomater.* **2013**, *9* (10), 8714–8721.

(47) Velikokhatnyi, O. I.; Kumta, P. N. First-principles studies on alloying and simplified thermodynamic aqueous chemical stability of calcium-, zinc-, aluminum-, yttrium- and iron-doped magnesium alloys. *Acta Biomater.* **2010**, *6* (5), 1698–1704.

(48) Gusieva, K.; Davies, C. H. J.; Scully, J. R.; Birbilis, N. Corrosion of magnesium alloys: the role of alloying. *Int. Mater. Rev.* **2015**, *60* (3), 169–194.

(49) Agnew, S. R.; Horton, J. A.; Yoo, M. H. Transmission electron microscopy investigation of  $\langle c+a \rangle$  dislocations in Mg and  $\alpha$ -solid solution Mg-Li alloys. *Metall. Mater. Trans. A* **2002**, *33* (3), 851–858.

(50) Lee, R. E.; Jones, W. J. D. Microplasticity and fatigue of some magnesium-lithium alloys. *J. Mater. Sci.* **1974**, *9* (3), 469–475.

(51) Kamado, S. Deformability and strengthening of superlight Mg-Li alloys. *Metall. Sci. Technol.* **1998**, *16* (1–2), 45–54.

(52) Hardie, D.; Parkins, R. N. Lattice spacing relationships in magnesium solid solutions. *Philos. Mag.* **1959**, *4* (43), 815–825.

(53) Song, Y. W.; Shan, D. Y.; Chen, R. S.; Han, E. H. Corrosion characterization of Mg-8Li alloy in NaCl solution. *Corros. Sci.* **2009**, *51* (5), 1087–1094.

(54) Shaw, C. A.; Tomljenovic, L. Aluminum in the central nervous system (CNS): toxicity in humans and animals, vaccine adjuvants, and autoimmunity. *Immunol. Res.* **2013**, *56* (2), 304–316.

(55) Kawahara, M. Effects of aluminum on the nervous system and its possible link with neurodegenerative diseases. *J. Alzheimer's Dis.* **2005**, *8* (2), 171–82.

(56) Ebina, Y.; Okada, S.; Hamazaki, S.; Midorikawa, O. Liver, kidney, and central nervous system toxicity of aluminum given intraperitoneally to rats: A multiple-dose subchronic study using aluminum nitilotriacetate. *Toxicol. Appl. Pharmacol.* **1984**, *75* (2), 211–218.

(57) Zhang, X.; Yuan, G.; Mao, L.; Niu, J.; Ding, W. Biocorrosion properties of as-extruded Mg-Nd-Zn-Zr alloy compared with commercial AZ31 and WE43 alloys. *Mater. Lett.* **2012**, *66* (1), 209–211.

(58) Fischer, J.; Pröfrock, D.; Hort, N.; Willumeit, R.; Feyerabend, F. Improved cytotoxicity testing of magnesium materials. *Mater. Sci. Eng., B* **2011**, *176* (11), 830–834.

(59) Wang, Z. H.; Yan, J.; Li, J. A.; Zheng, Q.; Wang, Z. G.; Zhang, X. N.; Zhang, S. X. Effects of biodegradable Mg-6Zn alloy extracts on apoptosis of intestinal epithelial cells. *Mater. Sci. Eng., B* **2012**, *177* (4), 388–393.

(60) Chen, Y.; Yan, J.; Wang, X.; Yu, S.; Wang, Z.; Zhang, X.; Zhang, S.; Zheng, Y.; Zhao, C.; Zheng, Q. In vivo and in vitro evaluation of effects of Mg-6Zn alloy on apoptosis of common bile duct epithelial cell. *BioMetals* **2014**, *27* (6), 1217–1230.

(61) Wang, Z.; Zhang, X.; Chen, S.; Wang, D.; Wu, J.; Liang, T.; Liu, C. Lithium chloride inhibits vascular smooth muscle cell proliferation and migration and alleviates injury-induced neointimal hyperplasia via induction of PGC-1 $\alpha$ . *PLoS One* **2013**, *8* (1), e55471.

(62) Myrissa, A.; Agha, N. A.; Lu, Y.; Martinelli, E.; Eichler, J.; Szakacs, G.; Kleinhans, C.; Willumeit-Römer, R.; Schafer, U.; Weinberg, A. M. In vitro and in vivo comparison of binary Mg alloys and pure Mg. *Mater. Sci. Eng., C* **2016**, *61*, 865–874.

(63) Witte, F.; Fischer, J.; Nellesen, J.; Crostack, H. A.; Kaese, V.; Pisch, A.; Beckmann, F.; Windhagen, H. In vitro and in vivo corrosion measurements of magnesium alloys. *Biomaterials* **2006**, *27* (7), 1013–1018.

(64) Xue, D.; Yun, Y. H.; Tan, Z.; Dong, Z.; Schulz, M. J. In vivo and in vitro degradation behavior of magnesium alloys as biomaterials. *J. Mater. Sci. Technol.* **2012**, *28* (3), 261–267.